

Active learning for photonic crystals

Ryan Lopez,^{1,*} Charlotte Loh,² Rumen Dangovski,² and Marin Soljačić¹

¹*Department of Physics, Massachusetts Institute of Technology, Cambridge, Massachusetts, USA*

²*Department of Electrical Engineering and Computer Science, Massachusetts Institute of Technology, Cambridge, Massachusetts, USA*

Active learning for photonic crystals explores the integration of analytic approximate Bayesian last layer neural networks (LL-BNNs) with uncertainty-driven sample selection to accelerate photonic band gap prediction. We employ an analytic LL-BNN formulation, corresponding to the infinite Monte Carlo sample limit, to obtain uncertainty estimates that are strongly correlated with the true predictive error on unlabeled candidate structures. These uncertainty scores drive an active learning strategy that prioritizes the most informative simulations during training. Applied to the task of predicting band gap sizes in two-dimensional, two-tone photonic crystals, our approach achieves up to a $2.6\times$ reduction in required training data compared to a random sampling baseline while maintaining predictive accuracy. The efficiency gains arise from concentrating computational resources on high uncertainty regions of the design space rather than sampling uniformly. Given the substantial cost of full band structure simulations, especially in three dimensions, this data efficiency enables rapid and scalable surrogate modeling. Our results suggest that analytic LL-BNN based active learning can substantially accelerate topological optimization and inverse design workflows for photonic crystals, and more broadly, offers a general framework for data efficient regression across scientific machine learning domains.

I. INTRODUCTION

Modern scientific and engineering workflows increasingly depend on machine-learning surrogates to circumvent the steep computational or experimental costs of high-fidelity simulations. For instance, in photonics, computing the full band structure of a photonic crystal can be computationally expensive, severely limiting the exploration of large design spaces and slowing inverse-design cycles [1]. Data-efficient strategies that strategically select only the most informative simulations are therefore essential to accelerate discovery and optimization in such domains.

Active learning (AL) addresses this challenge by iteratively querying labels for unlabeled points deemed most informative by a model [2]. Early pool-based AL in classification relied on uncertainty sampling, selecting points near decision boundaries via margin or entropy measures, to achieve significant label savings on image and text datasets [3, 4]. Batch active learning extends the standard AL setting by querying multiple points simultaneously rather than a single example per iteration. Supporting larger batch sizes is important in modern training pipelines because model updates are expensive, but naïvely selecting the top- k uncertain points often yields redundant and highly correlated samples [5]. To overcome this problem, recent batch AL methods have integrated diversity constraints with uncertainty. For example, BatchBALD extended pointwise mutual information to batches through a greedy $(1 - 1/e)$ approximation using MC-dropout BNNs [6], whereas BADGE derives pseudo-labels and applies k -means++ clustering on gradient embeddings for joint uncertainty–diversity sampling [7]. Batch Active Learning at Scale further combines margin based uncertainty with round-robin style sampling from clusters to support massive batch sizes (up to millions) with provable label-complexity bounds [8], and principled determinantal point processes have been efficiently approximated with MCMC [9]. Scalability via posterior-sparse approximations,

akin to Bayesian coresets, has also been demonstrated for both classification and regression settings [10]. Semi-supervised hybrids further ameliorate computational costs by pretraining encoders on unlabeled data before fitting a stochastic prediction head [11].

Despite these advances in classification, many scientific applications require continuous predictions rather than discrete labels. Pool-based batch AL for regression has been explored through “black-box” methods like B3AL, which uses kernelized embeddings of virtual ensembles to generalize white-box acquisition functions to arbitrary models [12], and Gaussian-process acquisitions such as maximum expected prediction error (MEPE) have been applied to machine-learning force-field training [13]. In chemical reactivity and potential-energy surface sampling, committee-variance sampling with message-passing neural nets has shown dramatic efficiency gains by focusing on high-variance molecular configurations [14]. Active learning has recently been applied to improve data efficiency in nanophotonic design problems, including surrogate modeling for PDE-based metasurface components and large-scale inverse design across diverse design spaces [15, 16]. However, these approaches focus on metasurface design rather than analytic uncertainty–driven regression for photonic-crystal band-gap prediction.

Approximate Bayesian neural networks (BNNs) offer principled uncertainty quantification, but conventional approaches rely on Monte Carlo sampling, often via MC-dropout or deep ensembles, with tens to hundreds of forward passes per candidate, which can be prohibitive in high-throughput settings [17, 18]. Approximate last layer Bayesian neural networks (LL-BNNs), in contrast, permit a closed-form, infinite-MC-limit solution: both the predictive variance and the Kullback–Leibler (KL) regularizer admit analytic expressions, eliminating sampling noise and reducing acquisition overhead to a single forward pass plus a few matrix operations. Recent work on variational Bayesian last layers (VBLL) generalizes this formulation by introducing a deterministic variational objective that achieves sampling-free inference with only quadratic complexity in the last-layer width [19]. Complementary directions such as evidential deep learning provide

* rlopez@mit.edu

non-Bayesian yet efficient uncertainty estimation by directly predicting distributional evidence parameters, enabling well-calibrated uncertainty at nearly no additional inference cost and powering uncertainty-guided active learning in molecular property prediction [20].

In this work, we introduce an analytic LL-BNN active learning framework tailored to regression of two-dimensional photonic crystal band gaps. We train the full network jointly, feature extractor and approximate Bayesian last layer, on an initial pool of 50 samples and iteratively select the next 50 most uncertain candidates by evaluating the closed form variance. On a dataset of 11,376 two-tone 2D photonic crystals, our uncertainty-driven sampling achieves up to $2.6\times$ data savings compared to random selection. To our knowledge, this is the first application of analytic last-layer approximate BNN active learning to photonic-crystal regression, and it offers a practical, data-efficient surrogate for photonic band gap estimations. A high-level overview of our active learning workflow is shown in Figure 1.

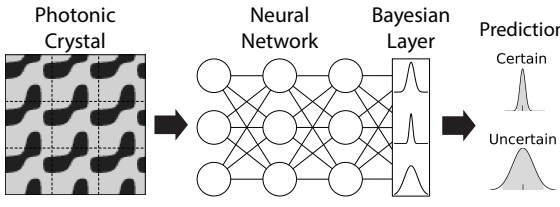


Figure 1. Active-Learning Pipeline for 2D Photonic-Crystal Band-Gap Prediction. Starting from the dielectric-constant map of a 2D two-tone photonic-crystal unit cell (augmented via symmetry operations), we feed each sample into a deep neural network whose final layer is approximate Bayesian. In this last layer, each weight and bias is treated as a Gaussian random variable, so a single input yields a predictive distribution rather than a point estimate. When evaluating unlabeled candidates, we compute the output variance as an uncertainty score and select the highest-variance samples for expensive band-structure simulations. By iteratively adding only the most informative points, the model rapidly improves its accuracy with far fewer training examples.

II. METHODS

A. Approximate bayesian last layer

An approximate Bayesian last layer can be appended to any neural network, both trained jointly, to provide uncertainty estimates with minimal overhead. Denote by $x \in \mathbb{R}^d$ the deterministic features from the backbone and $y \in \mathbb{R}$ the regression target. The last layer computes $W^\top x + b$ where the weight vector $W \in \mathbb{R}^d$ and bias $b \in \mathbb{R}$ are treated as random variables. Each component is distributed independently as

$$W_i \sim \mathcal{N}(\mu_{w,i}, \sigma_{w,i}^2), \quad b \sim \mathcal{N}(\mu_b, \sigma_b^2) \quad (1)$$

where $\mu_w, \sigma_w \in \mathbb{R}^d$ and $\mu_b, \sigma_b \in \mathbb{R}$ are trainable parameters. These independent Gaussians together define the variational posterior $q(W, b)$. We then place a standard normal prior over the variables:

$$p(W, b) = \mathcal{N}\left(\begin{bmatrix} W \\ b \end{bmatrix}; 0, I\right) \quad (2)$$

and train by minimizing a loss inspired by the negative evidence-lower-bound (ELBO):

$$\mathcal{L} = \underbrace{\mathbb{E}_{q(W,b)}[(y - W^\top x - b)^2]}_{\mathcal{L}_{\text{pred}}} + \underbrace{D_{\text{KL}}[q(W,b) \parallel p(W,b)]}_{\mathcal{L}_{\text{KL}}} \quad (3)$$

with $D_{\text{KL}}(\cdot)$ denoting the Kullback-Leibler divergence. Since this is the only Bayesian layer, the predictive-loss term admits an analytic closed form (the $\text{MC} \rightarrow \infty$ limit of sampling):

$$\mathcal{L}_{\text{pred}} = \mathbb{E}_{q(W,b)}[(y - W^\top x - b)^2] = (y - \mu_w^\top x - \mu_b)^2 + x^\top \Sigma_w x + \sigma_b^2, \quad (4)$$

where $\Sigma_w = \text{diag}(\sigma_{w,1}^2, \dots, \sigma_{w,d}^2)$.

Similarly, the KL term over independent Gaussians is

$$\mathcal{L}_{\text{KL}} = \sum_{i=1}^d D_{\text{KL}}(\mathcal{N}(\mu_{w,i}, \sigma_{w,i}^2) \parallel \mathcal{N}(0, 1)) + D_{\text{KL}}(\mathcal{N}(\mu_b, \sigma_b^2) \parallel \mathcal{N}(0, 1)) \quad (5)$$

$$= \sum_{i=1}^d \left[-\ln \sigma_{w,i} + \frac{\sigma_{w,i}^2 + \mu_{w,i}^2 - 1}{2} \right] + \left[-\ln \sigma_b + \frac{\sigma_b^2 - 1}{2} \right]. \quad (6)$$

From (3), large posterior variances $\{\sigma_{w,i}^2, \sigma_b^2\}$ incur both higher predictive variance and a larger KL penalty, so the model learns to keep uncertainty low where possible. In particular, the per-input uncertainty score

$$s(x) = \text{Var}[W^\top x + b] = x^\top \Sigma_w x + \sigma_b^2 \quad (7)$$

is available in closed form and used for uncertainty-sampling. Sampling the highest-variance point is equivalent to greedily minimizing the model's parameter uncertainty; further details are provided in Appendix VIA.

B. Uncertainty active learning

We use Algorithm 1 to intelligently select samples for training. Uncertainty sampling typically outperforms random sampling because it actively selects the examples on which the current model is least confident, thereby maximizing information gain per label. By focusing on high-uncertainty points, often near poorly explored regions of the input space, the model learns from the most ambiguous or informative data first, which accelerates error reduction and improves data efficiency. In contrast, random sampling treats all unlabeled points equally, wasting valuable labeling budget on regions the model already understands well. As a result, uncertainty sampling can achieve a given level of accuracy with far fewer labeled examples, making it especially advantageous when labels are costly or slow to obtain.

Algorithm 1 Active learning for regression

```

1: Input: Initial labeled set  $L$ , unlabeled set  $U$ , budget  $B$ , query
batch size  $q$ 
2: while  $B > 0$  do
3:   Train model  $M$  on  $L$ 
4:   for each sample  $x \in U$  do
5:     Compute uncertainty score  $s(x)$  using  $M$ 
6:   end for
7:   Select a subset  $S \subset U$  of  $q$  samples with highest  $s(x)$ 
8:   Query oracle to obtain true labels for  $S$ 
9:   Update labeled set:  $L \leftarrow L \cup S$ 
10:  Update unlabeled pool:  $U \leftarrow U \setminus S$ 
11:  Update budget:  $B \leftarrow B - q$ 
12: end while
13: Output: Final model  $M$  trained on  $L$ 

```

C. Neural network architecture and training

For our prediction neural network we use a deterministic feature-extraction network followed by an analytic approximate Bayesian layer. The feature network takes as input a single-channel 32×32 discretized permittivity map representing a two-dimensional photonic crystal unit cell. The feature extractor consists of two convolutional layers with 32 and 64 channels, respectively, each using 3×3 kernels and ReLU activations. The second convolutional layer is followed by 2×2 max pooling. The resulting feature maps are flattened and passed through a fully connected hidden layer with 128 output units and ReLU activation. This is then passed to the final approximate Bayesian layer that maps the 128-dimensional feature vector to a distribution of scalar outputs.

Training is performed within an active learning loop. The model is initialized using an initial labeled set of 50 samples and retrained from scratch at each iteration as new samples are acquired. At each iteration, 50 unlabeled samples are selected based on predictive uncertainty and added to the training set. Mini-batches of size 64 are used, and models are trained for 300 epochs per iteration using the Adadelta optimizer with an initial learning rate of 0.1. A cosine annealing learning-rate schedule is applied over the full training horizon.

III. DATASET

We use the same 2D photonic crystal dataset generated in Loh et al.[1]; further details can be found in that work. Each 2D square PhC unit cell is parameterized by taking the level set of a Fourier-sum function, summing nine plane waves with random complex coefficients, and thresholding it to produce a two-tone permittivity profile $\epsilon(r) \in \{\epsilon_1, \epsilon_2\}$ with ϵ_i sampled uniformly in $[1, 20]$. This yields distinct 32×32 pixel unit-cell images. For each selected cell, the transverse-magnetic band structure is computed using MPB with a 25×25 plane-wave basis and a 25×25 k -point grid, from which the largest band gap in the first 10 bands is directly extracted and used as the scalar regression label for training.

To further enhance data efficiency, we exploit the intrinsic symmetries of the square photonic-crystal lattice, also used in Loh et al.[1]. Because the electromagnetic band struc-

ture is invariant under rigid motions that preserve the geometry—specifically, translations, rotations by 90° , 180° , and 270° , as well as mirror reflections across the horizontal and vertical axes—we use these operations as physics-preserving data augmentations (see Figure 2). This ensures that the network learns features that are robust to lattice orientation and spatial placement, while effectively expanding the diversity of the training distribution without altering the underlying band-gap labels. Such augmentation improves generalization and accelerates convergence by enforcing the physical invariances of the system directly through the data.

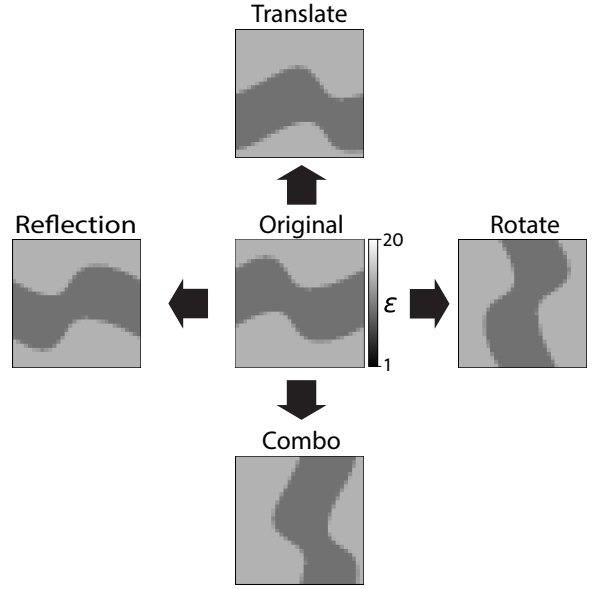


Figure 2. Symmetry-preserving data augmentation for 2D photonic crystal unit cells. Rotations, reflections, and translations of the 32×32 permittivity maps leave the photonic band structure unchanged. During training, random combinations of these transformations are applied to each sample, effectively enlarging the dataset while enforcing physical invariance of the band gap labels.

IV. RESULTS**A. Uncertainty estimation**

Our active learning strategy hinges on selecting samples with the highest model uncertainty, so it is only necessary that our approximate Bayesian last layer produces uncertainty estimates that rank points in order of true error, even if those estimates are not numerically perfectly calibrated. To verify this monotonicity, we proceed as follows:

- 1. Predictive statistics.** For each test input x , record the model's predictive standard deviation $s(x)$ and its squared error $(y - \hat{y})^2$.
- 2. Sorting and binning.** Sort all test samples by increasing $s(x)$, then partition them into bins of 100 samples each.

3. **Bin-wise MSE.** Within each bin, compute the mean squared error $\frac{1}{|\mathcal{B}|} \sum_{i \in \mathcal{B}} (y_i - \hat{y}_i)^2$.
4. **Monotonicity metric.** Compute the Spearman rank correlation between the sorted sample index and the mean squared errors to quantify their monotonic relationship.

Figure 3 displays one such calibration curve: bins with higher predictive standard deviation exhibit proportionally higher true mean square error (MSE). This confirms that, even with a modestly performing model, our uncertainty estimates reliably identify the samples on which the model is most likely to err, showing that uncertainty-driven sampling is likely to outperform random selection. Spearman's rank correlation coefficient, which ranges from -1 for a perfect inverse monotonic relationship to $+1$ for a perfect direct monotonic relationship, quantifies how well higher predicted uncertainties correspond to larger true errors; the Spearman values throughout all active learning iterations are plotted in Figure 4.

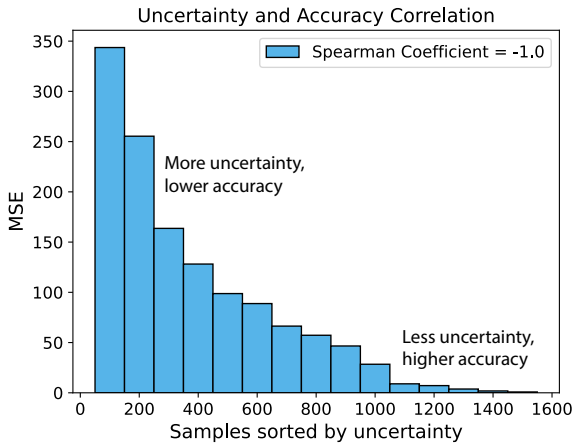


Figure 3. BNN Uncertainty Calibration. After training on 50 randomly selected samples, we evaluate our approximate Bayesian last layer on the held-out test set. For each test point, we compute the predictive standard deviation $s(x)$ and the squared error $(y - \hat{y})^2$. We then sort all test samples by $s(x)$, partition them into 15 bins of 100 samples each, and plot the mean squared error (MSE) of each bin along the sorted sample index. The clear downward trend shows that higher estimated uncertainty corresponds to larger true errors, confirming a strong monotonic relationship even when the overall model accuracy is low.

B. Performance curves

We evaluate active learning on a dataset of 11,376 two-tone, 2D photonic crystal unit cells, growing the training set from an initial pool of 50 up to 2,500 samples in increments of 50. At each iteration, we train the full network (including the Bayesian last layer), compute uncertainty scores for all unlabeled candidates, select the 50 samples with highest predictive variance, and retrain. Figure 5 plots the resulting test set mean squared error versus cumulative training size, comparing our uncertainty-driven acquisition to uniform random sampling (with matched random seeds and initial pools). Uncertainty

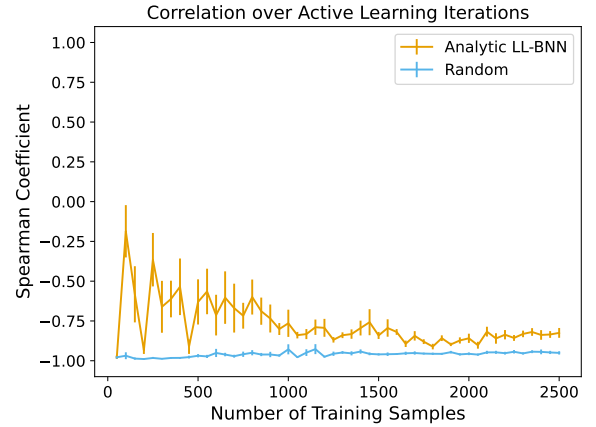


Figure 4. Spearman Coefficient over Active Learning. At each active learning step we compute the Spearman rank correlation on the test dataset. As it consistently remains negative, we see that the model's uncertainty is inversely correlated to true error through the wide range of training dataset sizes. We also note the uncertainty-based sample selection in the Analytic LL-BNN reduces the magnitude of this correlation, since -1 signifies perfect correlation.

sampling consistently outperforms random selection, reduces variability across runs, and achieves target accuracy with approximately 2.6 times fewer labeled examples. For a controlled comparison, the random sampling baseline uses the same network architecture and training protocol, differing only in the sampling strategy. The test set mean squared error is computed using the predictive mean of the model.

V. DISCUSSION

This study demonstrates that analytic approximate last-layer Bayesian neural networks (LL-BNNs) can serve as a practical engine for active learning in data-intensive photonics problems. By replacing Monte-Carlo sampling with a closed-form predictive variance, our approach avoids sampling noise and yields stable, deterministic uncertainty estimates, enabling reliable large-scale screening of candidate structures with a single forward pass. In the context of two-dimensional, two-tone photonic crystals, we find that uncertainty-driven acquisition reaches the same predictive accuracy as random sampling with roughly 2.6 times fewer labeled examples, translating to substantial reductions in simulation time and computational budget. Beyond band gap prediction, the ability to append an analytic approximate Bayesian last layer to an arbitrary feature extractor suggests a scalable path to data-efficient regression across diverse scientific domains.

While our results are encouraging, several limitations remain. The present framework uses pure uncertainty sampling without explicit diversity constraints, which can lead to redundant selections when highly uncertain samples cluster in similar regions of the input space. Incorporating batch-diverse acquisition functions such as determinantal point processes or BatchBALD could further improve performance in active-learning iterations. In addition, although our uncertainty es-

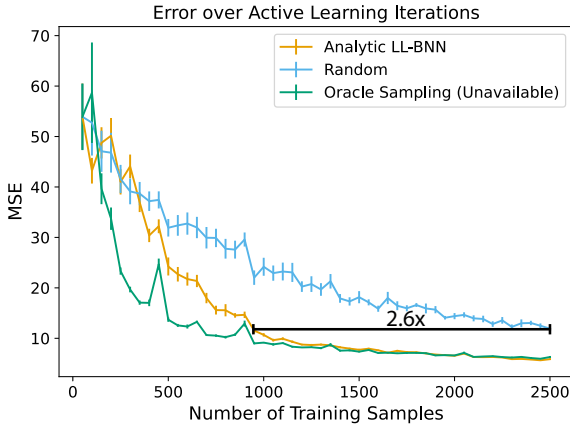


Figure 5. Comparison of Random vs Uncertainty-Driven Sampling. Test set MSE for photonic-crystal band-gap prediction as a function of total training samples, averaged over ten runs (each initialized with a different random pool of 50 examples). Blue shows standard random sampling; orange shows uncertainty sampling via our approximate Bayesian last layer. The green curve shows an “oracle” baseline that, at each iteration, greedily selects the 50 unlabeled samples with the highest true regression error—information unavailable in practice. This oracle is not globally optimal but provides an upper bound on what any greedy acquisition based on uncertainty could achieve. Error bars indicate standard error across runs. Uncertainty sampling not only achieves lower error at every budget level but also exhibits far less run-to-run variability and reaches the same accuracy as random sampling with roughly one-third the data.

timates rank samples accurately by true error, absolute calibration was not the focus of this study. For safety-critical applications or multi-objective optimization, improved calibration (e.g., via evidential deep learning [21] or temperature scaling [22]) may become important.

Future work could explore integrating this analytic LL-BNN active learning into full inverse-design loops for photonic crystals, where a surrogate model is repeatedly queried inside an optimizer. Because the Bayesian component is restricted to the last layer, the approach is compatible with more expressive feature extractors such as graph neural networks, transformers, or physics-informed architectures. Another promising direction is hybridizing uncertainty sampling with semi-supervised pretraining or active data augmentation to further reduce the initial labeled pool. Finally, benchmarking against Monte-Carlo-based BNNs and Gaussian-process acquisitions on three-dimensional photonic-crystal datasets would clarify the trade-offs between analytic variance, diversity, and scalability at larger problem sizes.

Overall, our results suggest that analytic LL-BNN active learning offers a simple yet powerful tool for data-efficient surrogate modeling. By combining principled uncertainty estimation with a lightweight implementation, the method opens the door to faster exploration and optimization of complex design spaces in photonics and other scientific disciplines.

FUNDING

We would like to thank the Dean of Science Fellowship for funding this study. This research was also sponsored in part by the United States Air Force Research Laboratory and the Department of the Air Force Artificial Intelligence Accelerator and was accomplished under Cooperative Agreement number FA8750-19-2-1000. The views and conclusions contained in this document are those of the authors and should not be interpreted as representing the official policies, either expressed or implied, of the Department of the Air Force or the US Government. The US Government is authorized to reproduce and distribute reprints for Government purposes notwithstanding any copyright notation herein. This material is also based upon work sponsored in part by the US Army DEVCOM ARL Army Research Office through the MIT Institute for Soldier Nanotechnologies under Cooperative Agreement number W911NF-23-2-0121, as well as MIT MGAIC and Shell Global.

ACKNOWLEDGEMENTS

We would like to thank MIT SuperCloud for computing resources and acknowledge ChatGPT for assistance with manuscript text editing.

DISCLOSURES

The authors declare no conflicts of interest.

DATA AVAILABILITY STATEMENT

Data and code underlying the results presented in this paper are available at

https://github.com/ryanlopezzz/photonics_al.

VI. APPENDIX

A. Information-theoretic active learning

Given model parameters θ (in our case $\mu_w, \sigma_w, \mu_b, \sigma_b$) and a labeled dataset D , we aim to select a new sample (x, y) such that the updated dataset D' minimizes the posterior entropy over the model parameters:

$$\arg \min_{(x,y)} H(\theta | D'). \quad (8)$$

Since the true label y is unknown, this objective can be reformulated as its expected counterpart:

$$\arg \max_x H(\theta | D) - \mathbb{E}_{y \sim p(y|x,D)} [H(\theta | y, x, D)], \quad (9)$$

which is equivalent to maximizing the conditional mutual information $I(\theta; y | x, D)$. This expression can also be rewritten

as:

$$\arg \max_x H(y|x, D) - \mathbb{E}_{\theta \sim p(\theta|D)}[H(y|x, \theta)]. \quad (10)$$

In our setting, the second term vanishes because each sampled model yields a deterministic prediction (i.e., $H(y|x, \theta) = 0$). Thus, the acquisition criterion simplifies to selecting the sample that maximizes predictive entropy:

$$\arg \max_x H(y|x, D). \quad (11)$$

For an approximate Bayesian neural network with a Gaussian last layer, the predictive distribution is given by

$$y = w^\top x + b \sim \mathcal{N}(\mu_{w,i}x_i + \mu_b, \sigma_{w,i}^2x_i^2 + \sigma_b^2).$$

The corresponding analytic expression for the predictive entropy is then

$$\begin{aligned} H(y|x, D) &= \frac{1}{2} \log[2\pi e (\sigma_{w,i}^2 x_i^2 + \sigma_b^2)] \\ &= \frac{1}{2} \log[2\pi e \cdot s(x)], \end{aligned} \quad (12)$$

where $s(x)$ denotes the predictive variance. Consequently, the greedy active learning strategy reduces to selecting the sample with the highest predictive uncertainty.

[1] C. Loh, T. Christensen, R. Dangovski, S. Kim, and M. Soljačić, Surrogate-and invariance-boosted contrastive learning for data-scarce applications in science, *Nature Communications* **13**, 4223 (2022).

[2] B. Settles, Active learning literature survey, University of Wisconsin, Madison (2009).

[3] D. D. Lewis, A sequential algorithm for training text classifiers: Corrigendum and additional data, in *AcM Sigir Forum*, Vol. 29 (ACM New York, NY, USA, 1995) pp. 13–19.

[4] S. Tong and D. Koller, Support vector machine active learning with applications to text classification, *Journal of machine learning research* **2**, 45 (2001).

[5] S. C. Hoi, R. Jin, and M. R. Lyu, Batch mode active learning with applications to text categorization and image retrieval, *IEEE Transactions on Knowledge and Data Engineering* **21**, 1233 (2009).

[6] A. Kirsch, J. Van Amersfoort, and Y. Gal, Batchbald: Efficient and diverse batch acquisition for deep bayesian active learning, *Advances in neural information processing systems* **32** (2019).

[7] J. T. Ash, C. Zhang, A. Krishnamurthy, J. Langford, and A. Agarwal, Deep batch active learning by diverse, uncertain gradient lower bounds, in *International Conference on Learning Representations* (2020).

[8] G. Citovsky, G. DeSalvo, C. Gentile, L. Karydas, A. Rajagopalan, A. Rostamizadeh, and S. Kumar, Batch active learning at scale, *Advances in Neural Information Processing Systems* **34**, 11933 (2021).

[9] E. Büyükkö, K. Wang, N. Anari, and D. Sadigh, Batch active learning using determinantal point processes, *arXiv preprint arXiv:1906.07975* (2019).

[10] R. Pinsler, J. Gordon, E. Nalisnick, and J. M. Hernández-Lobato, Bayesian batch active learning as sparse subset approximation, *Advances in neural information processing systems* **32** (2019).

[11] F. B. Smith, A. Foster, and T. Rainforth, Making better use of unlabelled data in bayesian active learning, in *International conference on artificial intelligence and statistics* (PMLR, 2024) pp. 847–855.

[12] A. Kirsch, Black-box batch active learning for regression, *Transactions on Machine Learning Research* (2023).

[13] A. Thomas-Mitchell, G. Hawe, and P. L. Popelier, Calibration of uncertainty in the active learning of machine learning force fields, *Machine Learning: Science and Technology* **4**, 045034 (2023).

[14] X. Guan, J. P. Heindel, T. Ko, C. Yang, and T. Head-Gordon, Using machine learning to go beyond potential energy surface benchmarking for chemical reactivity, *Nature Computational Science* **3**, 965 (2023).

[15] R. Pestourie, Y. Mroueh, T. V. Nguyen, P. Das, and S. G. Johnson, Active learning of deep surrogates for pdes: application to metasurface design, *npj Computational Materials* **6**, 164 (2020).

[16] S. Singh, R. Kumar, P. Singh, and R. Hegde, Active learning for efficient nanophotonics inverse design in large and diverse design spaces, *Opt. Express* **33**, 20308 (2025).

[17] Y. Gal, R. Islam, and Z. Ghahramani, Deep bayesian active learning with image data, in *International conference on machine learning* (PMLR, 2017) pp. 1183–1192.

[18] V. Rakesh and S. Jain, Efficacy of bayesian neural networks in active learning, in *Proceedings of the IEEE/CVF conference on computer vision and pattern recognition* (2021) pp. 2601–2609.

[19] J. Harrison, J. Willes, and J. Snoek, Variational bayesian last layers, in *The Twelfth International Conference on Learning Representations* (2024).

[20] A. P. Soleimany, A. Amini, S. Goldman, D. Rus, S. N. Bhatia, and C. W. Coley, Evidential deep learning for guided molecular property prediction and discovery, *ACS central science* **7**, 1356 (2021).

[21] A. Amini, W. Schwarting, A. Soleimany, and D. Rus, Deep evidential regression, *Advances in neural information processing systems* **33**, 14927 (2020).

[22] C. Guo, G. Pleiss, Y. Sun, and K. Q. Weinberger, On calibration of modern neural networks, in *International conference on machine learning* (PMLR, 2017) pp. 1321–1330.